SAND2019-11613J

# Imaging Effectiveness Calculator for Non-Design Microscope Samples

STEPHEN M. ANTHONY,[1,*] PHILIP R. MILLER,[2], JERILYN A. TIMLIN,[1] AND RONEN POLSKY[2]

[1] *Bioenergy and Defense Technologies Department, Sandia National Laboratories, 1515 Eubank Blvd. SE, Albuquerque, NM 87123*
[2] *Nano and Micro Sensors Department, Sandia National Laboratories, 1515 Eubank Blvd. SE, Albuquerque, NM 87123*
[*] *smantho@sandia.gov*

**Abstract:** When attempting to integrate single molecule fluorescence microscopy with microfabricated devices such as microfluidic channels, fabrication constraints may prevent using traditional coverslips. Instead, the fabricated devices may require imaging through material with a different thickness or index of refraction. Altering either can easily reduce the quality of the image formation (measured by the Strehl ratio) by a factor of two or more, reducing the signal-to-noise ratio accordingly. In such cases, successful detection of single molecule fluorescence may prove difficult or impossible. Here we provide software to calculate the effect of non-design materials upon the Strehl ratio or ensquared energy and explore the impact of common materials used in microfabrication.

## 1. Introduction

Individually, both single molecule microscopy [1] and microfluidics [2] have commanded substantial interest in recent years. The combination of the two, single-molecule fluorescence detection in microfluidic channels, has been suggested to be "the Holy Grail" of micro total analysis systems ($\mu$TAS) [3]. While single molecule fluorescence detection in microfluidic channels has been demonstrated on a number of occasions [4, 5], several factors render these experiments particularly challenging. To begin with, the signal-to-noise ratio (SNR) is frequently extremely low when imaging single fluorophores, such that a SNR of >5 is considered a high SNR and a SNR of 2 is not uncommon [6]. Additionally, microfluidic devices made with either polydimethylsiloxane (PDMS) or plastic often have lower SNR due to the inherent fluorescence of these compounds. As such, single molecule fluorescence microscopy inherently operates near the limits of detection [6]. However, one factor that is often overlooked in this field is the impact of non-design coverslips on the microscope image formation.

The high numerical aperture (NA) objectives commonly used for single molecule fluorescence imaging are precision optics, most of which are designed to provide optimal performance with borosilicate coverslips 170 $\mu$m thick (#1.5 coverslips). Deviations from the specified coverslip generally introduce optical aberrations, particularly spherical aberration, which decrease the image quality. Unfortunately, borosilicate glass does not readily lend itself to microfabrication. On the other hand, while silicon is the preferred material for microfabrication, it is opaque to visible light. As a result, when imaging through a microfabricated material is required, some of the most commonly selected materials are quartz, fused silica, Borofloat 33, or PDMS. The index of refraction of these compounds ( 1.4 to 1.47 at 532 nm) differs substantially from that of a design coverslip (1.526 at 532 nm).

Though this difference in index of refraction compared to design coverslips is small, most microscopists know that image quality degrades substantially when imaging several microns into an aqueous sample using an oil immersion objective. As such, it should not be surprising

that the quality of focus can degrade even more significantly when using a non-design coverslip. Admittedly, the difference between the index of refraction of design and non-design coverslips is roughly three times less than the difference between the index of refraction of immersion oil ($n_{oil} \approx 1.518$) and water ($n_{water} \approx 1.33$). On the other hand, imaging into an aqueous solution results in an index of refraction mismatch for only a few microns, whereas using a non-design coverslip results in an index of refraction mismatch for a layer over 100 $\mu$m thick.

Complicating the matter, using a non-design coverslip may alter the ideal focal position. By altering the focal position of the microscope (the thickness of the immersion oil layer) it may be possible to partially cancel the aberrations introduced by the non-design coverslip [7, 8]. While the aberrations are unlikely to perfectly cancel, "Rayleigh's quarter wavelength rule states that if the maximum value of an aberration function is less than a quarter of an illumination wavelength... the intensity at the focus is changed by a small amount which is considered to be tolerable." [9] As such, even though altering the thickness of the immersion oil may only partially cancel the aberrations, in some circumstances that may be sufficient to restore sharp focus.

An analytical model exists for the aberrations introduced by differences between the actual acquisition conditions and the design conditions of microscope objectives [10]. While the initial model by Gibson and Lanni was based upon scalar diffraction theory, it has since been extended to vector diffraction theory [7]. For our purposes, though, scalar diffraction theory is sufficient and is used for all calculations in this work. In short, using existing optical theory it is possible to compute the entire point spread function (PSF) for non-design coverslips of arbitrary thickness and focal depth. While the theory is well developed, translating from the theory to practical effects on imaging is beyond the expertise of many microscope users.

Two convenient measures of the focal quality, the Strehl ratio and the ensquared energy, can be readily calculated from the PSF. While related, each of these measures offers advantages. The Strehl ratio can be defined as the ratio of the peak intensity of the aberrated point source relative to the peak intensity of the corresponding diffraction limited system for the same aperture [11]. As such, the Strehl ratio for any system conveniently ranges between 0 and 1, where the Strehl ratio equals 1 only for ideal optical systems. One common criterion for a well-functioning optical system is Marechal's criterion, which requires the Strehl ratio to be greater than 0.8 [9]. When used as designed, a typical research-grade microscope will have a Strehl ratio of almost exactly 1.

An alternate measure of the focal quality is the ensquared energy, defined as the fraction of the total PSF intensity which is within a centered square of a specified size (centered on the centroid of the PSF). Possible values for the ensquared energy also range from 0 to 1, but in this case the ensquared energy for any PSF will be 1 if the square is sufficiently big. In order to compare the quality of image formation for different PSFs, it is necessary to specify a fixed size for the square. For digital microscopy, a convenient size square to employ is the detector pixel size; throughout the rest of this work, the ensquared energy will refer to the ensquared energy for a pixel. In some ways, the ensquared energy per pixel is a more practical measure than the Strehl ratio. By accounting for the pixel size, this measure quantifies the impact on the peak signal that would be experimentally observed. For example, if the detector has particularly large pixels, it is possible that the PSF would be almost entirely contained within a single pixel (ensquared energy $\approx 1$) even when the Strehl ratio reduces from 1.0 to 0.75. At the same time, the Strehl ratio is often easier to interpret; the ideal Strehl ratio is always 1.0, but the ensquared energy per pixel may be much less than 1, even for perfect optics.

While the Strehl ratio and the ensquared energy provide convenient measures of the imaging quality, how non-design parameters in the Gibson and Lanni PSF effect these measures is not intuitive. Determining the Gibson and Lanni PSF requires calculating the integral of a complex valued function containing a Bessel function. Therefore, determining the Strehl ratio and ensquared energy is not straightforward and may fall outside the normal areas of expertise of scientists simply interested in knowing how using a non-design coverslip will affect their

image quality. While a convenient PSF calculator exists which supports multiple PSF models including the Gibson and Lanni model [12], the implementation is intended for the common case of focusing on fluorophores away from the coverslip. As such, while this tool allows the depth inside the sample to be varied, it does not allow for non-design coverslips. A more recent work allows all the Gibson-Lanni parameters to be varied and the PSF to be rapidly calculated [13], but is not optimized for multiple calculations with different coverslip conditions. In this current work, we explore the effect of common microfabrication materials on the image quality, including whether image quality can be restored by independently altering the thickness of the non-design coverslip and the focal depth. Additionally, we develop and provide software (Code 1, Ref. [14]) to calculate the Gibson and Lanni PSF, Strehl ratio, and ensquared energy, allowing non-design immersion, coverslip, and sample layers. While primarily directed at microfabricated channels where it is more difficult to use commercially available coverslips, this calculator is relevant whenever non-design coverslips or other optical windows or media are used.

## 2. Gibson and Lanni Model

The Gibson and Lanni PSF model is a generalization of the Born and Wolf PSF model allowing for refractive index mismatches between the design and experimental optical system. A detailed analysis of the relationship between the Gibson-Lanni and Born-Wolf models is available in Appendix A of [12]. In brief, the Gibson-Lanni model is a laterally shift invariant model which includes a phase term accounting for spherical aberrations up to second order. Imaging off the optical axis would be expected to introduce additional aberrations not accounted for by the Gibson-Lanni model. The spherical aberrations may be induced by differences between the design and experimental optical system in the refractive indices, the layer thicknesses, or a combination of the two. The typical formulation assumes three optical layers, corresponding to the microscope sample or specimen, the coverslip, and the immersion media (See Figure 1). The standard Gibson and Lanni model uses scalar diffraction theory and assumes that the index of refraction is constant within a layer. These assumptions and approximations are sufficient for single molecule imaging in microfluidic devices and are used throughout this work. However, the Gibson and Lanni model has been extended to vector diffraction theory, [7] arbitrary numbers of layers, [15] and variable refractive indices within layers [15].

Throughout this work, we will only consider the intensity of the PSF as this is what is typically measured in the microscope, disregarding the phase. Since the Gibson-Lanni PSF is shift invariant in the lateral direction, we will express it in terms of $r(\theta)$, where $r(\theta)$ corresponds to the apparent lateral position relative to the point source in the image plane. The Gibson-Lanni PSF is given by

$$
\begin{aligned}
I(\theta) &= \left| C \int_0^1 J_0\left[kNA\rho r\right] \times e^{iW\rho} \times \rho d\rho \right|^2, \qquad (1)\\
r &= \sqrt{x^2 + y^2},\\
W(\rho) &= k\left[ n_s t_s \sqrt{1 - \left(\frac{NA\rho}{n_s}\right)^2} + n_g t_g \sqrt{1 - \left(\frac{NA\rho}{n_g}\right)^2} + n_i t_i \sqrt{1 - \left(\frac{NA\rho}{n_i}\right)^2} \right.\\
&\quad \left. - n_g^* t_g^* \sqrt{1 - \left(\frac{NA\rho}{n_g^*}\right)^2} - n_i^* t_i^* \sqrt{1 - \left(\frac{NA\rho}{n_i^*}\right)^2} \right],
\end{aligned}
$$

where the terms in Equation 1 are defined in Table 1.

Microscope objectives are designed to either image at the interface between the sample and the coverslip or to image into a sample whose index of refraction equals that of the immersion medium.

| Term | Description |
|---|---|
| $I(\theta)$ | Intensity of the PSF for the specified parameters |
| $C$ | A normalizing constant |
| $J_0(\theta)$ | Zeroth order Bessel function of the first kind |
| $k$ | $\frac{2\pi}{\lambda}$ |
| $\lambda$ | Wavelength of the emitted light (in vacuum) |
| $NA$ | Numerical aperture of the microscope |
| $x, y$ | The apparent lateral positions relative to the point source in the image plane |
| $r$ | The apparent radial position relative to the point source in the image plane |
| $i$ | $\sqrt{-1}$ |
| $n_s$ | Refractive index of the actual sample (or specimen) layer |
| $n_s^*$ | Refractive index of the design sample layer |
| $t_s$ | Thickness of the actual sample layer imaged through (axial position of the point source within the sample layer) |
| $t_s^*$ | Thickness of the design sample layer imaged through |
| $n_g$ | Refractive index of the actual coverslip |
| $n_g^*$ | Refractive index of the design coverslip |
| $t_g$ | Thickness of the actual coverslip |
| $t_g^*$ | Thickness of the design coverslip |
| $n_i$ | Refractive index of the actual immersion media layer |
| $n_i^*$ | Refractive index of the design immersion media layer |
| $t_i$ | Thickness of the actual immersion media layer |
| $t_i^*$ | Thickness of the design immersion media layer |
| $W$ | The Gibson and Lanni phase aberration |

Table 1: Description of terms used in Equation 1

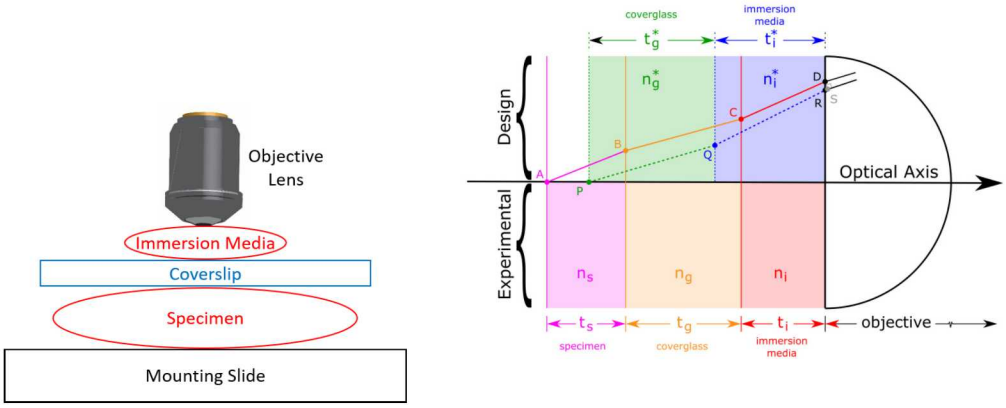


(a) (b)

Fig. 1: (a) Schematic diagram of the three optical layers accounted for by the Gibson-Lanni model: the immersion media, the coverslip or coverglass, and the specimen layers. (b) For each layer, the design and actual (or experimental) refractive index and thickness must be specified. The design conditions for the sample layer are not shown, as the design thickness of the sample layer is 0. Design (dashed line) and actual (solid line) rays entering the front of the microscope objective travel different optical paths. The optical path difference between the design and actual ray can be computed as OPD = [ABCD] - [PQRS].

An example of the latter case is using a water immersion objective to image into an aqueous sample in order to be able to focus effectively deeper into the sample. From the perspective of the Gibson-Lanni model, though, the two cases are equivalent although in reality there would, of course, be slight differences not captured by the model including Fresnel reflections at the extra interfaces. The Fresnel reflections also result in slight differences between the excitation and detection PSFs [16]. Examining the model shows that all layers with the same index of refraction can effectively be combined, acting equivalently to a single layer with the same total thickness and index of refraction. Similarly, the order of the layers does not matter for the Gibson-Lanni model. As a consequence, there is no need to include terms for the design sample layer thickness in $W$; either its thickness is zero or it has the same index of refraction as the immersion layer and can be combined with that layer.

When considering PSF generation, one factor which warrants special consideration is the critical angle. Examination of Snell's law for refraction immediately shows that when a ray of light propagates from an optically denser medium into a less dense one, a maximum angle exists beyond which refraction cannot occur. This critical angle is defined as $\theta_{critical} = \arcsin\left(\frac{n_1}{n_2}\right)$, where $n_2 > n_1$, and above the critical angle total internal reflection occurs. When attempting to image single molecule fluorescence, high numerical aperture microscope objectives are generally employed, where the numerical aperture (NA) is defined as "the sine of the angular semiaperture in the object space multiplied by the refractive index of the object space, $NA = n \sin(\theta)$." [11]

Since the value of the sine cannot exceed 1, when imaging far into a sample the maximum effective NA is clearly limited to the index of refraction of the sample. However, while the index of refraction of aqueous samples is $n_{water} \approx 1.33$, high NA objectives used in biology to image these samples often have nominal NA values from 1.4 to 1.46. Why the apparent discrepancy between the nominal objective NA and its effective NA? First, if the goal when designing the objectives is to collect the maximum amount of light, the numerical aperture of the objective

should be at least equal to the refractive index of the object space. While exceeding the refractive index of the object space does not result in greater far-field light collection, anything less reduces the amount of light captured. Meanwhile, the exact target value varies between samples; while the refractive index of pure water is approximately 1.33, the refractive index of normal cells is typically 1.35-1.37 while the refractive index of cancerous cells often approaches 1.4 [17]. So, while the higher objective NA may not improve the image quality for some samples, it is advantageous because it allows one to obtain optimum images from all samples.

Additionally, the highest NA objectives are often designed to allow objective-based total internal reflection fluorescence (TIRF) microscopy. Objective-based TIRF microscopy is only possible if the nominal objective NA is higher than the index of refraction of the sample layer, allowing total internal reflection to occur. Given the range of indices of refraction in biological samples, reliably obtaining TIRF conditions may be difficult unless the objective has an NA greater than or equal to 1.4. Moreover, objective-based TIRF is limited to imaging fluorophores which are very near the coverslip. For near-field imaging (whether TIRF or the subset of fluorophores in the near-field for epi-illumination), fluorescence is no longer strictly limited by the critical angle. Instead, the evanescent components of the fluorescent dipole can propagate directly into the coverslip as supercritical angular fluorescence (SAF) or "forbidden light" [18,19]. As such, while for far-field optics the effective NA is limited to the index of refraction of the sample medium, for near-field optics NA values above the index of refraction of the sample medium can result in enhanced light collection.

Unfortunately, examination of Equation 1 easily shows that the Gibson-Lanni PSF model does not support supercritical emission. If the NA is larger than the index of refraction of any of the layers, the corresponding square root term will not be real-valued. At first glance, it might appear tempting to simply drop the problematic first square root term in $W(\rho)$ of Equation 1 for near field imaging, thinking that might allow the Gibson-Lanni PSF to support SAF. However, another aspect of SAF which has been long known is that fluorophores in the near-field emit a disproportionate portion of their fluorescence into the medium with the higher index of refraction, where the radiation distribution has been previously worked out [20–24]. More recently, the strong dependence of SAF upon the separation between the fluorophore and the coverslip has been employed to allow simultaneous observation and discrimination between near-field and far-field phenomena [25].

Extending the Gibson-Lanni PSF to support super-critical imaging would therefore require significant modification, outside the scope of this work. Since our software (Code 1) employs the Gibson-Lanni PSF model, it naturally inherits the limitations of the Gibson-Lanni PSF. In light of these limitations, when the software provided with this work(Code 1) is given the objective NA as an input, for convenience the effective far-field NA for the PSF is calculated by the software, limiting the NA to the lesser of the nominal NA or the lowest index of refraction. A mathematically equivalent way of limiting the effective NA is used by Li et al. [13] They reduce the integration range of $\rho$, such that the integration range is not always $\rho \in [0, 1]$. As such, our software should only be considered truly accurate for far-field imaging; while including a TIRF setting which is necessarily near-field, the TIRF setting only enforces a negligible thickness to the sample layer but does not account for effects like SAF that are not supported by the Gibson-Lanni model.

## 3. Microfabrication Materials Indices of Refraction

For convenience, the indices of refraction of several materials commonly employed in biological microscopy or microfabrication are collected here. Of course, the refractive index of materials varies with the wavelength of the light, a phenomenon known as dispersion. For purposes of this work we have standardized on using the indices of refraction at 532 nm, a common laser line.

Table 2 provides the indices of refraction for various compositions of borosilicate glass, the

| Borosilicate Composition | $n_{532}$ | $n_e$ | $V_e$ |
|---|---|---|---|
| Ohara- S-BSM36 (borosilicate, medium index) | 1.6461 [26] | | |
| Ohara- S-BSM2 (borosilicate, medium index) | 1.6109 [26] | | |
| Zeiss High Performance Coverslips | 1.5263 | 1.5255 [27] | 56 [27] |
| Schott D263M (borosilicate) | 1.5263 | 1.5255 [28] | 55 [28] |
| Schott - BK7G18 (borosilicate crown) | 1.5225 [26] | | |
| Ohara - BSL22 (borosilicate, low-index) | 1.5208 [26] | | |
| Hoya - BSC7 (borosilicate crown) | 1.5195 [26] | | |
| Hikari - J-BK7A (borosilicate crown) | 1.5195 [26] | | |
| Schott - N-BK7® (borosilicate crown) | 1.5195 [26] | | |
| Ohara - S-BSL7 (borosilicate, low-index) | 1.5190 [26] | | |
| Sumita - K-BK7 (borosilicate crown) | 1.5190 [26] | | |
| Ohara - BSL3 (borosilicate, low-index) | 1.5009 [26] | | |
| Schott - N-BK10 (borosilicate crown) | 1.5003 [26] | | |

Table 2: Indices of refraction at 532 nm for various compositions of borosilicate glass. For compounds where the index of refraction at 532 nm was not directly available, it was calculated using the index of refraction and reciprocal dispersion (Abbe number) at a different wavelength (See Appendix 6).

material typically used for microscope coverslips. The range of refractive indices in this table, from 1.5190 to 1.6109 at 532 nm, shows that for precision optical systems specifying the general type of glass is insufficient. Instead, the exact material employed or the refractive index must be specified. Of the borosilicate glasses listed in Table 2, only Schott D263M and the material used in Zeiss high performance coverslips meet the ISO 8255-1 specifications for microscope coverslips. [29] Table 3 provides the indices of refraction for a number of materials commonly used in microfabrication or microscopy.

## 4. Imaging Quality

Figure 2 shows the effect of non-design coverslip thickness and index of refraction on the Strehl ratio and ensquared energy at the best focus. All calculations were performed for a 60× oil immersion TIRF objective (Olympus Plan APO, $NA$ 1.45) with a working distance of 150 $\mu$m and designed for use with #1.5 coverslips. Calculations were performed for TIRF excitation into an aqueous solution ($n_s$ = 1.3337), calculating the PSF and imaging quality for fluorophores emitting at 532 nm. The pixel size of the simulated detector was 16 $\mu$m, chosen to match the EMCCD in our TIRF microscope (Andor Technologies, Inc, iXon 887). For each coverslip thickness of the various compounds, the best focus was determined by calculating the immersion oil thickness for standard immersion oil ($n_i = n_i^* = 1.519$) which produced the highest Strehl ratio. For materials where $n_g \leq n_i^*$, the Strehl ratio and ensquared energy abruptly decrease when the coverslip thickness exceeds 250 $\mu$m, where the exact transition depends upon the material. Detailed examination shows that unsurprisingly, as the coverslip thickness increases,

| Material | $n_{532}$ | $n_d$ | $V_d$ | $n_e$ | $V_e$ |
|---|---|---|---|---|---|
| Sapphire | 1.7718 [26] | | | | |
| Hoya Sd2 | 1.534 | 1.531 [30] | 59 [30] | | |
| ISO 8255-1 Coverslips | 1.5263 | | | 1.5255 [28] | 56 [28] |
| Soda Lime | 1.5261 [26] | | | | |
| Immersion oil | 1.5190 | | | 1.5180 [31] | 44 [31] |
| Borofloat® 33 | 1.4737 | | | 1.47311 [32] | 65.41 [32] |
| Fused Silica | 1.4607 [26] | | | | |
| Quartz | 1.4607 [26] | | | | |
| PDMS | ≈1.43 [26] | | | | |
| Cancerous Cells | 1.4 [17] | | | | |
| Normal Cells | 1.35-1.37 [17] | | | | |
| Water | 1.3337 [26] | | | | |

Table 3: Indices of refraction at 532 nm for various materials. For compounds where the index of refraction at 532 nm was not directly available, it was calculated using the index of refraction and reciprocal dispersion (Abbe number) at a different wavelength (See Appendix 6). Note that as seen in Table 2, the index of refraction can vary even within identically named materials (e.g. borosilicate glass, soda lime glass). As such, the indices of refraction in this table may only represent particular examples of a material.

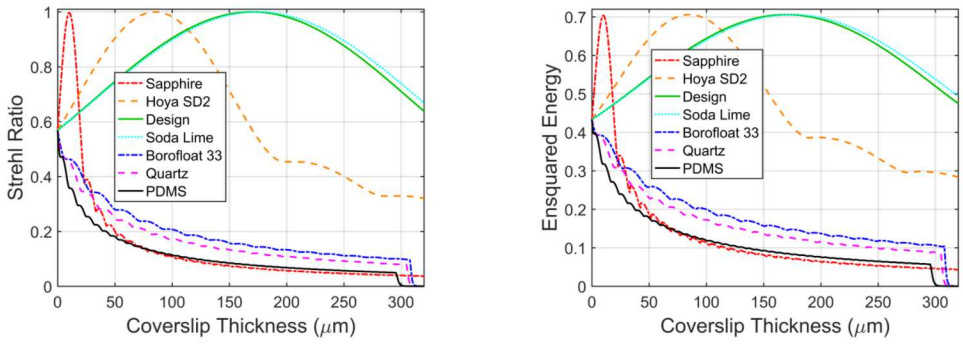


(a) (b)

Fig. 2: The Strehl ratio (a) and ensquared energy (b) calculated for a variety of potential coverslip materials at the best focus (optimum immersion oil thickness).

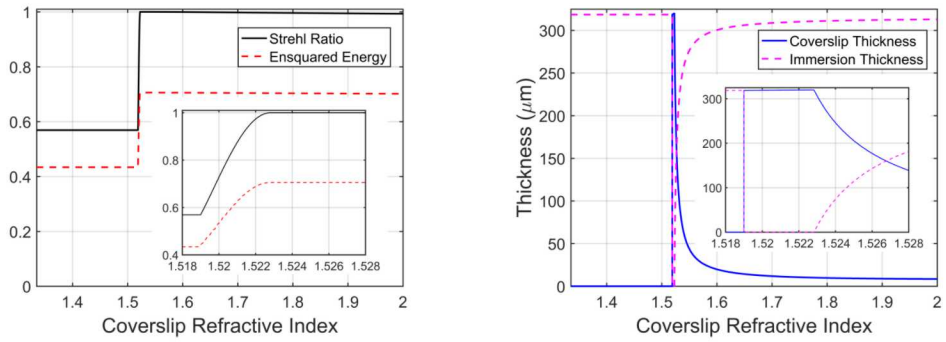


(a) (b)

Fig. 3: (a) The best obtainable Strehl ratio and ensquared energy depending upon the refractive index of the coverslip. (b) The coverslip and immersion oil thickness required to maximize the Strehl ratio depending upon the refractive index of the coverslip. The insets zoom in on the rapidly changing region when the coverslip refractive index varies from 1.518 to 1.528.

the optimum immersion oil thickness (best focus) occurs at an ever-decreasing immersion oil thickness. At some point, the optimum immersion oil thickness reaches zero. At that point, it is no longer possible to decrease the immersion oil thickness to compensate for increasing the coverslip thickness. As such, the amount of spherical aberration increases rapidly from that point, resulting in an abrupt drop in the Strehl ratio.

When varying the index of refraction of the coverslip, two clearly distinct ranges are observed: when $n_g \leq n_i^*$, and when $n_g > n_i^*$ (see Figure 3a). In the former case, obtaining a high Strehl ratio (above 0.8, Marechal's criterion) is theoretically impossible, and the optimum coverslip thickness is zero (see Figure 3b). In this region, the refractive index of both the immersion oil ($n_i^*$) and actual coverslip ($n_g$) differ from that of the design coverslip ($n_g^*$), so replacing any portion of the design coverslip with either of these materials will induce spherical aberration. However, since both $n_i^*$ and $n_g$ are less than $n_g^*$, both will produce the same sign of spherical aberration. As such, replacing part of the design coverslip layer with each material offers no benefit as no portion of the spherical aberration from these materials would cancel. Therefore, optimum imaging when $n_g \leq n_i^*$ is obtained by replacing the entirety of the design coverslip layer with immersion oil as the mismatch between $n_i^*$ and $n_g^*$ is less than the mismatch between $n_g$ and $n_g^*$. The boundary where $n_g = n_i^*$ represents a special case; here, the index of refraction of the actual coverslip exactly matches the index of refraction of the immersion oil, so the two are perfectly interchangeable.

In the alternate case when $n_g > n_i^*$, a non-zero coverslip thickness will maximize the Strehl ratio and in many cases a high Strehl ratio is theoretically possible. When $n_i^* < n_g^* < n_g$, reducing the actual coverslip thickness compared to the design coverslip thickness results in two regions of non-design index of refraction. In one of the regions, some of the design coverslip has been replaced with non-design coverslip, increasing the index of refraction. In the other region, some of the design coverslip has been replaced with immersion oil, increasing the index of refraction. While both regions will produce spherical aberration, since their sign is different the spherical aberrations will partially cancel each other. A similar phenomenon occurs when employing a non-design coverslip whose index of refraction is between that of the design coverslip and the immersion oil. In this subcase, decreasing the immersion oil thickness and increasing the coverslip thickness results in two regions of non-design index of refraction, where once again the sign of the mismatch differs between the two regions.

Figure 3 shows, however, that compensating for higher refractive index coverslips can proceed for much longer than lower refractive index coverslips. The better ability to compensate for coverslip refractive index increases is a result of the requirement that the total optical distance must remain relatively constant for the microscope objective to be in focus. As such, two constraints dictate the optimum coverslip thickness: the need to maintain a roughly constant total optical thickness and the need to minimize the total spherical aberrations. When the coverslip refractive index increases, constant optical thickness is maintained by decreasing the coverslip thickness and increasing the immersion oil thickness. While the amount of aberration per unit of coverslip thickness increases, the spherical aberration induced by the coverslip increases very slowly since its thickness is simultaneously decreasing. In contrast, when the coverslip refractive index decreases from its design value, balancing the two constraints requires the immersion oil thickness to fall rapidly. However, once the immersion oil thickness reaches zero, it cannot decrease further. Once that point is reached, further decreases in the coverslip refractive index can no longer be compensated for by decreasing the immersion oil thickness. As such, the minimum total spherical aberration rises rapidly and the Strehl ratio drops until $n_g = N_i^*$.

This analysis also suggests some potential options for improving the Strehl ratio when imaging either when $n_g \leq n_i^*$ or far into a sample where $n_s < n_i^*$. In either case, offsetting spherical aberrations are impossible to produce without introducing additional non-design elements. For both cases, using a non-design immersion oil where $n_i > N_i^*$ would introduce spherical aberrations of the opposite sign, which could potentially partially cancel and reduce the overall aberration. When $n_s < n_i^*$, another possible option would be to use a thicker coverslip than specified by the microscope objective, effectively replacing some of the immersion layer with coverslip.

Even when it is theoretically possible to maintain a high Strehl ratio when $n_i^* < n_g$, in practice that may not always prove possible. Examining Figure 3b reveals that depending upon the actual coverslip index of refraction, obtaining the optimum Strehl ratio may require an implausibly thin coverslip or immersion oil layer. For a sapphire coverslip to satisfy Marechal's criterion, the coverslip would need to be less than 20 $\mu$m thick (see Figure 2a). Employing such a thin coverslip would not generally be feasible, as a coverslip that thin would be incredibly fragile, difficult to fabricate and prone to breakage if used. On the other hand, when $n_g$ is only slightly greater than $n_i^*$, the optimum immersion oil thickness approaches 0. As the desired immersion oil thickness decreases, the risk of crashing the microscope objective into the coverslip increases dramatically. Additionally, beyond a certain point the viscosity of the immersion oil will make it difficult to decrease the immersion oil thickness without waiting a long time for it to reach equilibrium.

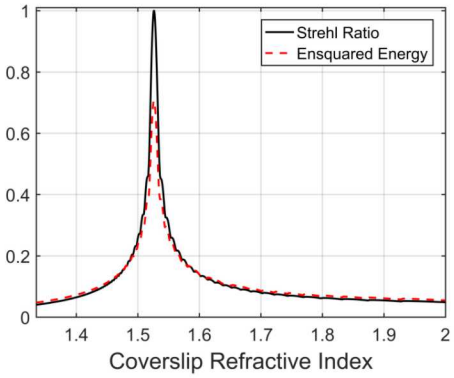


Fig. 4: The best obtainable Strehl ratio and ensquared energy for a 170 $\mu$m coverslip depending upon the refractive index of the coverslip.

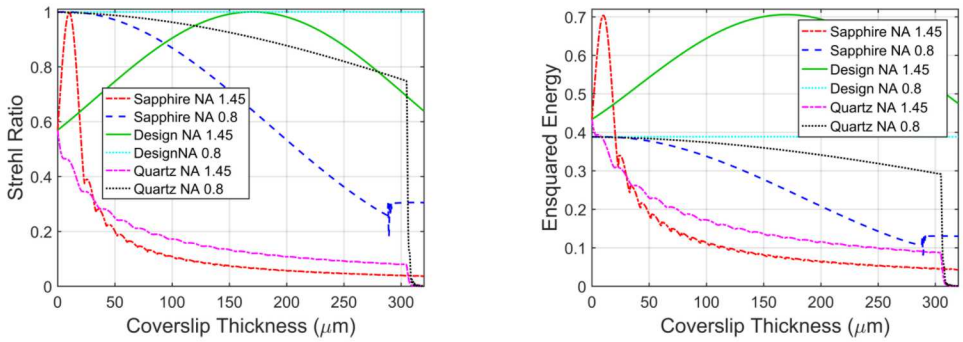


(a) (b)

Fig. 5: The Strehl ratio (a) and ensquared energy (b) calculated for a variety of potential coverslip materials at the best focus (optimum immersion oil thickness) for objectives with two different numerical aperture ($NA$) values. Aside from altering the NA and the coverslip index of refraction (material dependent), no other parameters were varied between simulations. Note that for an $NA$ 1.45 objective imaging into an aqueous solution, the effective $NA$ is limited to the index of refraction of the water, 1.3337.

Practical limitations are likely to be a minimum coverslip thickness of around 50-75 $\mu$m and a minimum immersion oil thickness of around 40-80 $\mu$m. As such, it can also be useful to consider what Strehl ratio can be obtained for a coverslip of design thickness (170 $\mu$m) as the index of refraction is varied (see Figure 4). While Figure 4 illustrates the effect of a mismatch in index of refraction of the coverslip while otherwise obeying the design constraints, a similar effect would be observed for a mismatch in index of refraction of the immersion oil. Since the refractive index of immersion oil is temperature dependent, imaging at 37°C as is commonly employed for imaging of live cells in biological applications using standard immersion oil (designed for 23°C) would have a similar effect, explaining why special immersion oil designed for imaging at 37°C is available. Note that this effect can also be modeled by the software developed in this work (Code 1); while the software does not include a temperature term, once the refractive index at a given temperature is determined, the code can calculate the impact of the refractive index mismatch.

The amount of spherical aberration depends strongly on the numerical aperture; since the range of angles of incident light is much higher for high $NA$ objectives, aberrations are much more pronounced. Figure 5 shows that for an objective with an $NA$ of 0.8, imaging quality (as measured by either the Strehl ratio or ensquared energy) does not vary much between design and non-design coverslips. Figure 5 also highlights an important difference between the Strehl ratio and ensquared energy. While the maximum Strehl ratio is the same for the design coverslip regardless of $NA$, the maximum ensquared energy decreases from 0.7 to 0.4. This difference reflects the fact that the Strehl ratio measures peak intensity relative to a diffraction limited spot for the same $NA$, effectively compensating for changes in NA. In general, the Strehl ratio is more convenient for evaluating performance for a given microscope objective under different conditions. However, Figure 4 shows that even for a single microscope objective, the Strehl ratio and ensquared energy are not perfectly correlated. When trying to determine the effect changing an imaging parameter will have on the observed signal-to-noise ratio, the ensquared energy is a more reliable measure.

The extensive availability and common use of quartz coverslips could erroneously lead researchers to assume that quartz coverslips are generally fine for imaging. From a microfabrication standpoint, quartz is much more commonly employed than borosilicate or soda lime glass, which

would also tend to favor its selection. However, Figure 2b shows that using a quartz coverslip with an $NA$ 1.45 objective will result in a roughly fivefold reduction in the ensquared energy (and signal-to-noise ratio). Why would anyone use quartz coverslips if it can degrade imaging performance so substantially? To begin with, the UV absorption of standard microscope coverslips makes quartz coverslips a necessity when imaging in the UV region of the spectrum. Similarly, quartz coverslips are commonly used for near-infrared excited Raman microscopy due to the high background signal from impurities in borosilicate coverslips. Additionally, in many circumstances the reduction in signal can either be tolerated, compensated for, or is otherwise less significant. In particular, Figure 5b indicates that for an $NA$ 0.8 objective, when using a quartz coverslip, the ensquared energy is >90% of the ensquared energy for the design coverslip.

In fact, the ensquared energy for a 170 $\mu$m quartz coverslip is actually higher for an $NA$ 0.8 objective than for an $NA$ 1.45 objective. Since the definition of high $NA$ is fuzzy, depending upon the $NA$, quartz coverslips can in some conditions be suitable for high $NA$ imaging. Similarly, while signal-to-noise ratio is a major concern when performing single molecule fluorescence imaging, limited signal is rarely a problem when performing bright field imaging. Finally, the signal-to-noise ratio can potentially be increased by either increasing the acquisition time or the laser excitation power. As such, it is possible to perform single-molecule fluorescence microscopy with an $NA$ 1.45 objective; it may simply require using 10 times higher laser intensity than typically employed [4]. However, while increasing the detector integration time or laser power may sometimes be possible, the associated drawbacks may make this infeasible. While increasing the laser power can increase the number of photons per second emitted by the fluorophore, doing so will also increase how quickly the fluorophore will photobleach. Increasing the integration time will increase the signal-to-noise at the expense of the temporal resolution. Additionally, single molecule fluorescence microscopy often requires careful attention to the photon budget; only a limited number of photons can be obtained from a fluorophore before it irreversibly bleaches [33]. In contrast, improving the ensquared energy improves the signal-to-noise ratio without consuming any additional photons from the limited photon budget.

The conclusions of this study were experimentally validated by comparing the observed PSFs for 175 nm orange fluorescent beads (Thermo Fisher PS-Speck Microscope Point Source Kit) in aqueous solution absorbed on coverslips, where the only difference between the experiments was whether a ISO 8255 borosilicate (measured thickness 179 $\mu$m, Fisherbrand Microscope Cover Glass 18 x 18 mm #1.5) or a quartz coverslip (measured thickness 192 $\mu$m, Chemglass Life Sciences Quartz Cover slips 19 x 19 mm; CGQ-0660-01) was employed. Imaging was performed using an Olympus Plan APO microscope objective with 60X magnification, 1.45 $NA$, and a 150 $\mu$m working distance mounted on an Olympus IX-71 inverted microscope with an attached iXon 887 emCCD (Andor Technologies, Inc.) with a 16 $\mu$m pixel size without gain. Epi-illumination was provided by a Coherent Sapphire 20 mW 532 nm laser; to minimize photobleaching and avoid saturating the detector, the laser power was reduced using neutral density filters such that the incident laser power into the microscope was measured as 9.8 $\mu$W. Figure 6 contains representative images showing that imaging the beads through quartz rather than through a standard coverslip results in a much dimmer PSF (lower ensquared energy). Each image was cropped to center the PSF, and the minimum value within the cropped region was subtracted to correct for any dark offset and background.

While calculations using our software showed that the ensquared energy for point sources should be 0.70 for the glass slide and 0.12 for the quartz slide, quantitative comparison between theory and experiment was complicated by the fact that while the PS-Speck beads employed are highly uniform in size (175 nm ± 5 nm), they are not intended as a fluorescent intensity standard. As such, intensity varies significantly between beads even within the same sample (e.g. Figure 6a vs 6b, Figure 6c vs. 6d), where inter-bead intensity variations by a factor of two are often observed. Unfortunately, beads designed as fluorescence intensity standards are

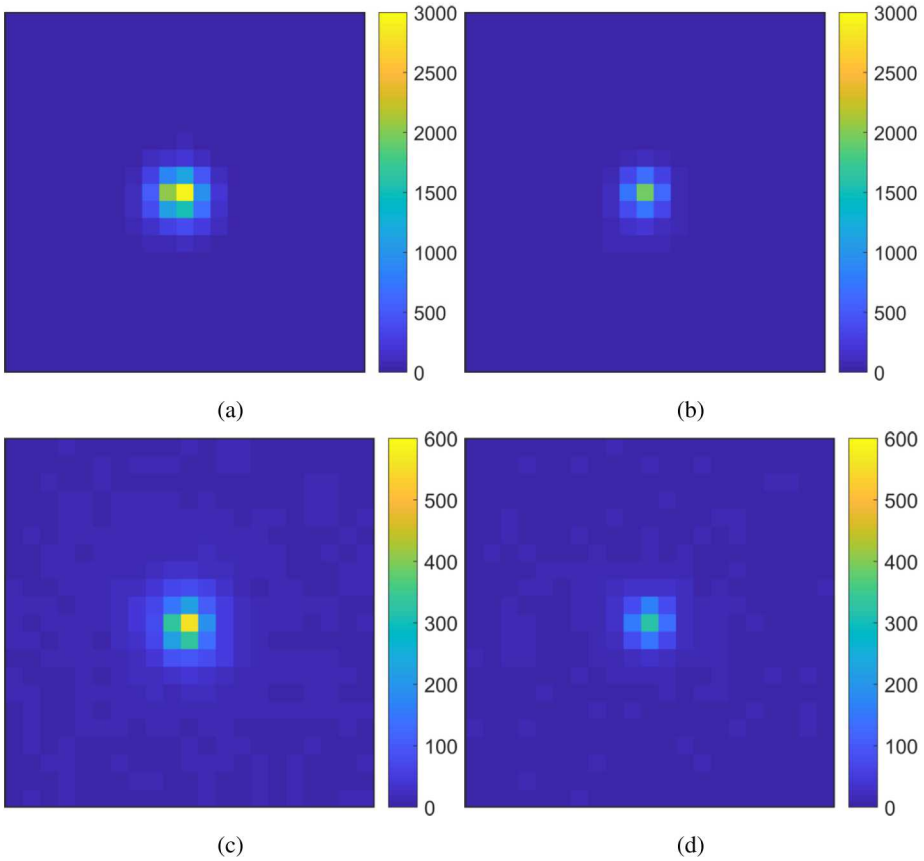


Fig. 6: Representative pseudo-colored images of 175 nm fluorescent beads in aqueous solution images on a,b) an ISO 8255 borosilicate coverslip 179 $\mu$m thick or c,d) a quartz coverslip 192 $\mu$m thick. In accordance with theory, the observed PSF with the design coverslip is much brighter than for the quartz coverslip (note the difference in color scale between a,b and c,d). Further experimental details and discussion are provided in the text.

invariably several microns in size, preventing their use as sub-resolution point sources. In fact, approximate calculations showed that even the 175 nm size of the PS-Speck beads is sufficient to reduce the theoretical ensquared energy when imaging the beads through the glass coverslip from 0.70 to 0.62 and from 0.12 to 0.11 for the quartz coverslip. Therefore, while the experimental observations are consistent with theoretical expectations, thorough quantification verification was not possible.

## 5. Software

While the effect of several non-design materials was explored in this work, open source software (see Code 1) is provided allowing anyone to explore the effects of materials not considered here. The software was designed in Matlab R2017b (Mathworks, Natick, MA) on Windows 10, but should generally be compatible with other versions of Matlab regardless of operating system. Figure 7a shows a screenshot of the software interface and the automatically displayed results. Besides calculating the PSF, Strehl ratio, and ensquared energy for the exact refractive indices and layer thicknesses specified, the software automatically evaluates whether

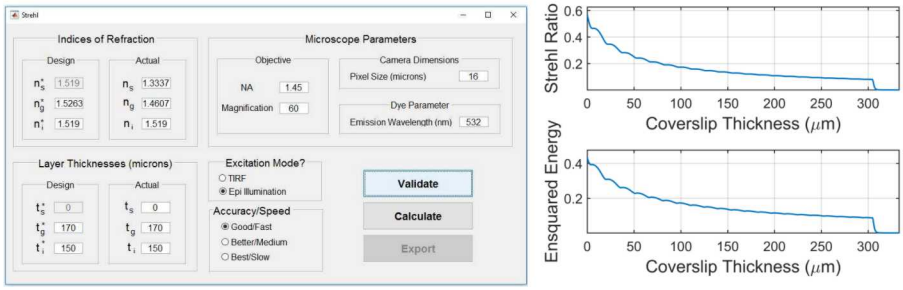


(a) (b)

Fig. 7: a) The graphical user interface (GUI) provided with the software developed in this work. The software is designed to make it easy for anyone to determine the effect of non-design imaging conditions on the resulting PSF. b) In addition to calculating the PSF, Strehl ratio, and ensquared energy for the exact conditions specified, the GUI also calculates the same values for the entire range of plausible coverslip thicknesses, automatically producing results like those shown in Figure 2, where the actual output of a) is shown here.

the Strehl ratio can be improved by using a coverslip with the specified actual index of refraction $n_g$ but a different coverslip thickness, allowing analysis like that in Figure 2 to be trivially performed for any material. The export button outputs the results of the calculation to the workspace as two structures. The variable "Sandia_Strehl_Specific_Condition_Results" provides all the processing parameters and results for the exact conditions specified in the GUI while "Sandia_Strehl_Scan_Thickness_Results" provides the same information for the range of coverslip thicknesses considered.

The code was designed in a modular fashion, where two functions of note are specifyStrehlDefaults.m and gibsonLanni.m. Editing specifyStrehlDefaults.m allows the default parameters used by the GUI to be adjusted to match the user's typical setup. Additionally, the default spacing to employ when evaluating possible coverslip thicknesses can be adjusted. The function gibsonLanni.m allows calculation of the Gibson-Lanni PSF, Strehl ratio, and ensquared energy independently of the GUI. In particular, it is designed to allow simultaneous calculation for vectors of different values of $t_i$, $t_g$, and $t_s$ and could easily be extended to do the same for any of the refractive indices or thicknesses. Additionally, two Abbe number calculators are provided, allowing calculation of the approximate index of refraction at any wavelength for compounds where only $n_d$ and $V_d$ or $n_e$ and $V_e$ are known.

Simultaneously calculating the Gibson-Lanni PSF for multiple different imaging conditions offers a major improvement in computational efficiency as the Bessel function portion of the integral only needs to be calculated once as it does not depend upon the optical path. Similarly, exploiting the radial symmetry of the PSF reduces the number of values for which the Bessel function must be determined. As such, while calculating the Bessel function is computationally expensive, calculating the Bessel function is less than 5% of the total computational time when calculating the Gibson-Lanni PSF for more than 280 optical path conditions. While our code is sufficiently fast for our purposes, determining the effect of a non-design material within under a minute, the code could likely be further optimized if desired. One obvious option would be switching to a GPU implementation in either CUDA or OpenCL, whether of just the Bessel function or a larger portion of the code. The current implementation uses standard Matlab (no mex files), and other languages might offer greater optimization. Finally, expansions allowing the elimination of the need to calculate integrals can offer substantial optimization, as demonstrated by Sheppard and Török [34]. One of the most recent optimizations to employ this strategy was

developed by Li et. al. [13] Their analysis showed that their software calculated the Gibson-Lanni PSF 64 times faster than the existing state-of-the-art algorithm [13]. Experimentation with their algorithm indicated that it produced excellent results for all values we tested, offering great benefits for tasks where PSF will need to be computed repeatedly such as deconvolution and particle localization. Incorporating their optimization into our code is straightforward and demonstrated an approximately threefold speed increase in total computational time. However, calculations performed by our code routinely employ parameters beyond the range for which the approximation error was reported [13]. Although it seems likely that the approximation error of Li et al.'s method would remain similarly insignificant for the entire range of parameters our code employs, we chose not to employ their approximation in our code at this time due to uncertainty about the approximation error for the full range of parameters employed in our code. Instead, we continue to calculate the integrals employing a discrete approximation.

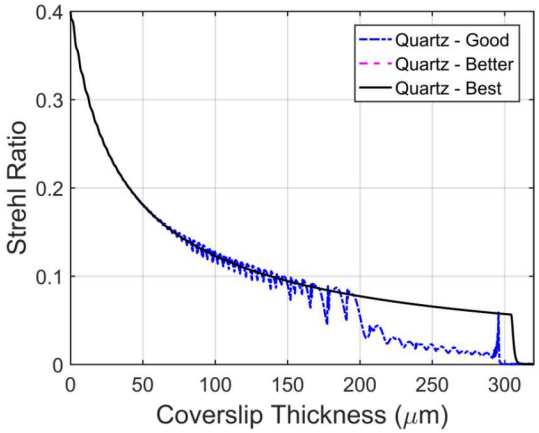


Fig. 8: The Strehl ratio calculated for a quartz coverslip under identical conditions except for the number of intervals into which rho was divided. Aside from changing the accuracy setting, setting the index of refraction of the actual coverslip to 1.4607 (quartz), and setting the coverslip thickness step size to 100 nm, the default GUI parameters were employed. Good accuracy subdivides $\rho$ into 1000 intervals, better into 10,000, and best into 100,000, where the calculation for those settings required 14.5 seconds, 153 seconds, and 1296 seconds respectively. For these parameters, increasing the accuracy from good to better is necessary; the good accuracy setting is inaccurate for these parameters, shown by the wild oscillations of the Strehl ratio (shown) or ensquared energy (not shown). However, increasing from better accuracy to best accuracy is unnecessary; while taking almost 10 times longer, the values are virtually identical. In fact, while both better and best are plotted in this Figure, the two are superimposed to the point that the better result cannot be seen.

One important criteria when calculating the PSF is the number of intervals to divide $\rho$ into for integration. Dividing $\rho$ into more intervals requires more computational time, but if $\rho$ is divided into too few intervals, the results will be inaccurate. However, the accuracy of the calculation does not improve linearly with the computational time; if $\rho$ is subdivided into too few intervals, the results can be wildly inaccurate. Building off Lord Rayleigh's quarter wavelength rule, if the optical path distance between two adjacent values of $\rho$ does not vary by more than $\frac{1}{4}$ wavelength, the resulting calculations are unlikely to deviate substantially from the exact result. For convenience, the software developed in this work automatically checks whether any deviations exceed $\frac{1}{4}$ wavelength, warning the user if that is the case and recommending reprocessing at the next higher level of accuracy. While for most calculations in this work the

good accuracy, fast setting would have been sufficient, for some materials like quartz, the better accuracy, medium speed setting was required. Therefore, for consistency all results in this work were calculated using the better accuracy setting unless otherwise specified. No results in this work required the best accuracy setting, and using a higher accuracy setting than required offers negligible benefit (see Figure 8). As such, the best accuracy setting should rarely be required but is included to allow calculations even further from the optical design.

## 6. Conclusions

We explored how common microfabrication materials and decisions can impact the image quality for single molecule fluorescence microscopy, as measured by both the ensquared energy and the Strehl ratio. Calculations are performed using the highly popular and experimentally validated Gibson-Lanni model. The impact of non-design coverslips becomes particularly significant for high numerical aperture objectives, the type typically employed for single molecule microscopy. In fact, the effect of numerical aperture is so significant that for quartz coverslips, the image formed by an $NA$ 0.8 objective would have a higher signal-to-noise ratio than the image formed with an otherwise equivalent $NA$ 1.4 objective, contrary to the general conception regarding numerical aperture. These results show care must be taken when considering any modifications to the imaging system; the effects are not always intuitive, particularly when multiple modifications are combined. Besides changes to materials employed, changes in temperature such as imaging at 37°C, a relatively common practice, can affect the refractive index and alter the image quality. Additionally, we provide convenient software to facilitate easy, fast, and accurate evaluation of these effects for arbitrary materials and conditions beyond those explored in this work.

The current calculator's accuracy is limited to far-field imaging in wide-field mode, and assumes that the microscope system is functioning properly when imaging design conditions. Extending the calculator to support confocal imaging, whether for single pinholes, spinning disk, or two photon imaging would be relatively straightforward as the Gibson-Lanni model for these modalities is well understood. Adapting the calculator to accurately support near-field imaging could also prove a valuable addition, although this would require extending the Gibson-Lanni model. Similarly, providing a related calculator to solve the reverse problem of identifying the parameters from a measured PSF. While previously demonstrated as possible by Haeberlé et al. [35], an optimized, modern calculator could be useful.

## Appendix A

In some cases, it was possible to directly obtain the index of refraction at 532 nm, $n_{532}$, from the reference. Other times, it was only possible to obtain the index of refraction and reciprocal dispersion (Abbe number) at a different wavelength. The formula for the Abbe number $V_d$ is

$$V_d = \frac{n_d - 1}{n_F - n_C}, \tag{2}$$

where $n_d$, $n_F$, and $n_C$ are the refractive indices at the helium d-line ($\lambda_d \approx 587.56$ nm), the hydrogen F-line ($\lambda_F \approx 486.13$ nm) and the hydrogen C-line ($\lambda_C \approx 656.27$ nm) respectively [36]. When the index of refraction and the reciprocal dispersion are known for a particular wavelength, the chromatic dispersion $\frac{\delta n}{\delta \lambda}$ can be calculated using the assumption that the dispersion is linear between the reference wavelengths in the denominator. For example, given $V_d$ and $n_d$ for a compound, the chromatic dispersion for that compound would be approximated as

$$\frac{\delta n_d}{\delta \lambda} \approx \frac{n_F - n_C}{\lambda_F - \lambda_C} = \frac{n_d - 1}{V_d \left(\lambda_F - \lambda_C\right)}. \tag{3}$$

Using the chromatic dispersion, the approximate index of refraction at any other wavelength can be calculated, where the index of refraction at 532 nm, $n_{532}$ would be calculated as

$$n_{532} \approx n_d + \frac{\delta n_d}{\delta \lambda} (532\text{nm} - \lambda_d) . \tag{4}$$

Of course, the accuracy of these approximations will depend upon how linear the dispersion is and will tend to be more accurate the closer the reference wavelength (e.g. $n_d$) is to the desired wavelength (e.g. $n_{532}$). Frequently, the refractive index and Abbe number are specified for a different wavelength such as the mercury e-line ($\lambda_e \approx 546.07$ nm) which is often easier to measure. The reference wavelengths and corresponding formula for the Abbe number $V_e$ are defined in ISO standard 7944 [37].

## Funding

Sandia National Laboratories Laboratory Directed Research and Development Program (180907)

## Acknowledgments

Danae Maes collected the experimental images. This paper describes objective technical results and analysis. Any subjective views or opinions that might be expressed in the paper do not necessarily represent the views of the U.S. Department of Energy or the United States Government. Sandia National Laboratories is a multimission laboratory managed and operated by National Technology and Engineering Solutions of Sandia LLC, a wholly owned subsidiary of Honeywell International Inc. for the U.S. Department of Energy's National Nuclear Security Administration under contract DE-NA0003525.

## References

1. M. J. Rust, M. Bates, and X. W. Zhuang, "Sub-diffraction-limit imaging by stochastic optical reconstruction microscopy (STORM)," Nat. Methods **3**, 793–795 (2006).
2. G. M. Whitesides, "The origins and the future of microfluidics," Nature **442**, 368–373 (2006).
3. P. S. Dittrich and A. Manz, "Single-molecule fluorescence detection in microfluidic channels - the holy grail in $\mu$TAS?" Anal. Bioanal. Chem. **382**, 1771–1782 (2005).
4. C. W. Hollars, J. Puls, O. Bakajin, B. Olsan, C. E. Talley, S. M. Lane, and T. Huser, "Bio-assay based on single molecule fluorescence detection in microfluidic channels," Anal. Bioanal. Chem. **385**, 1384–1388 (2006).
5. J. C. Roulet, R. Volkel, H. P. Herzig, E. Verpoorte, N. F. de Rooij, and R. Dandliker, "Fabrication of multilayer systems combining microfluidic and microoptical elements for fluorescence detection," J. Microelectromechanical Syst. **10**, 482–491 (2001).
6. I. Smal, M. Loog, W. Niessen, and E. Meijering, "Quantitative comparison of spot detection methods in fluorescence microscopy," IEEE Transactions on Med. Imaging **29**, 282–301 (2010).
7. O. Haeberlé, "Focusing of light through a stratified medium: a practical approach for computing microscope point spread functions. part I: Conventional microscopy," Opt. Commun. **216**, 55–63 (2003).
8. O. Haeberlé, "Focusing of light through a stratified medium: a practical approach for computing microscope point spread functions: Part ii: confocal and multiphoton microscopy," Opt. communications **235**, 1–10 (2004).
9. M. Gu, *Advanced Optical Imaging Theory*, Springer Series in Optical Sciences (Springer, Berlin, 1999), 1st ed.
10. S. F. Gibson and F. Lanni, "Experimental test of an analytical model of aberration in an oil-immersion objective lens used in 3-dimensional light-microscopy," J. Opt. Soc. Am. A-Optics Image Sci. Vis. **9**, 154–166 (1992).
11. M. Born and E. Wolf, *Principles of Optics* (Cambridge University Press, New York, 1999), 7th ed.
12. H. Kirshner, F. Aguet, D. Sage, and M. Unser, "3-D PSF fitting for fluorescence microscopy: implementation and localization application," J. Microsc. **249**, 13–25 (2013).
13. J. Li, F. Xue, and T. Blu, "Fast and accurate three-dimensional point spread function computation for fluorescence microscopy," J. Opt. Soc. Am. A **34**, 1029–1034 (2017).
14. S. M. Anthony, "Sandia strehl calculator version 1.0," https://osapublishing.figshare.com/s/c8010ddf610803b30bd6. Accessed on 2019-05-08.
15. S. Ghosh and C. Preza, "Fluorescence microscopy point spread function model accounting for aberrations due to refractive index variability within a specimen," J. biomedical optics **20**, 075003–075003 (2015).
16. O. Haeberlé, M. Ammar, H. Furukawa, K. Tenjimbayashi, and P. Török, "Point spread function of optical microscopes imaging through stratified media," Opt. Express **11**, 2964–2969 (2003).

17. X. J. Liang, A. Q. Liu, C. S. Lim, T. C. Ayi, and P. H. Yap, "Determining refractive index of single living cell using an integrated microchip," Sensors Actuators a-Physical **133**, 349–354 (2007).
18. L. Novotny, "Allowed and forbidden light in near-field optics. i. a single dipolar light source," JOSA A **14**, 91–104 (1997).
19. L. Novotny, "Allowed and forbidden light in near-field optics. ii. interacting dipolar particles," JOSA A **14**, 105–113 (1997).
20. W. Lukosz and R. Kunz, "Light emission by magnetic and electric dipoles close to a plane interface. i. total radiated power," JOSA **67**, 1607–1615 (1977).
21. W. Lukosz and R. Kunz, "Light emission by magnetic and electric dipoles close to a plane dielectric interface. ii. radiation patterns of perpendicular oriented dipoles," JOSA **67**, 1615–1619 (1977).
22. W. Lukosz, "Light emission by magnetic and electric dipoles close to a plane dielectric interface. iii. radiation patterns of dipoles with arbitrary orientation," JOSA **69**, 1495–1503 (1979).
23. J. Enderlein, T. Ruckstuhl, and S. Seeger, "Highly efficient optical detection of surface-generated fluorescence," Appl. optics **38**, 724–732 (1999).
24. T. Ruckstuhl, J. Enderlein, S. Jung, and S. Seeger, "Forbidden light detection from single molecules," Anal. chemistry **72**, 2117–2123 (2000).
25. T. Barroca, K. Balaa, J. Delahaye, S. Lévêque-Fort, and E. Fort, "Full-field supercritical angle fluorescence microscopy for live cell imaging," Opt. letters **36**, 3051–3053 (2011).
26. M. N. Polyanskiy, "Refractive index database," https://refractiveindex.info. Accessed on 2019-05-02.
27. L. Carl Zeiss, Microscopy, "Carl zeiss, microscopy, llc. - product search," https://www.micro-shop.zeiss.com/en/us/shop/search/cover%20glass. Accessed on 2019-05-02.
28. I. Ted Pella, "Microscope coverslip technical data," https://www.tedpella.com/histo_html/coverslip-info.htm. Accessed on 2019-05-02.
29. ISO Central Secretary, "Microscopes - Cover glasses – Part 1: Dimensional tolerances, thickness, and optical properties," Standard ISO 8255-1:2017, International Organization for Standardization, Geneva, CH (2017).
30. H. C. USA, "Sd-2 - glass substrate for silicon sensors," http://www.hoyaoptics.com/pdf/silicon_sensor.pdf. Accessed on 2019-05-02.
31. M. Abramowitz and M. W. Davidon, "Olympus microscopy resource center | microscope optical components - immersion media," http://olympus.magnet.fsu.edu/primer/anatomy/immersion.html. Accessed on 2019-05-02.
32. Schott, "Borofloat® 33 - optical properties," https://www.schott.com/d/borofloat/bde16ad3-70e5-48a0-b8ac-9146fcd34511/1.0/borofloat33_opt_en_web.pdf. Accessed on 2019-05-02.
33. J. R. Lakowicz, *Principles of fluorescence spectroscopy* (Springer Science & Business Media, 2007).
34. C. Sheppard and P. Török, "Efficient calculation of electromagnetic diffraction in optical systems using a multipole expansion," J. Mod. Opt. **44**, 803–818 (1997).
35. O. Haeberlé, F. Bicha, C. Simler, A. Dieterlen, C. Xu, B. Colicchio, S. Jacquey, and M.-P. Gramain, "Identification of acquisition parameters from the point spread function of a fluorescence microscope," Opt. communications **196**, 109–117 (2001).
36. R. R. Shannon, *The art and science of optical design* (Cambridge University Press, 1997).
37. ISO Central Secretary, "Optics and optical instruments – Reference wavelengths," Standard ISO 8255-1:2017, International Organization for Standardization, Geneva, CH (2017).